

Incommensurate antiferromagnetic order in CePtAl₃

M. Stekiel ^{1,2,*}, P. Čermák ^{1,3}, C. Franz ^{1,4}, W. Simeth ⁵, S. Weber,² E. Ressouche ⁶, W. Schmidt ⁷, K. Nemkovski ^{1,8},
H. Deng,^{1,9} A. Bauer ^{2,10}, C. Pfleiderer ^{2,10,11} and A. Schneidewind ¹

¹Jülich Centre for Neutron Science (JCNS) at Heinz Maier-Leibnitz Zentrum (MLZ),
Forschungszentrum Jülich GmbH, Lichtenbergstr. 1, D-85747 Garching, Germany

²Physik-Department, Technische Universität München, D-85748 Garching, Germany

³Charles University, Faculty of Mathematics and Physics, Department of Condensed Matter Physics,
Ke Karlovu 5, 121 16 Praha, Czech Republic

⁴MLZ, Technische Universität München, D-85748 Garching, Germany

⁵Paul Scherrer Institut, Villigen, Switzerland

⁶University Grenoble Alpes, French Alternative Energies and Atomic Energy Commission (CEA), Interdisciplinary Research Institute
of Grenoble (IRIG), Modeling and Exploration of Materials (MEM), Magnetism and Neutron Diffraction (MDN), 38000 Grenoble, France

⁷JCNS at Institute Laue-Langevin (ILL), Forschungszentrum Jülich GmbH, 38042 Grenoble, France

⁸ISIS Neutron and Muon Source, Science and Technology Facilities Council (STFC) Rutherford Appleton Laboratory,
Harwell Campus, Didcot, Oxon OX11 0QX, United Kingdom

⁹Institut für Kristallographie at MLZ, North Rhine-Westphalia Technical University (RWTH) Aachen,
Lichtenbergstrasse 1, D-85747 Garching, Germany

¹⁰Center for Quantum Engineering (ZQE), Technische Universität München, 85748 Garching, Germany

¹¹Munich Center for Quantum Science and Technology (MCQST), Technische Universität München, 85748 Garching, Germany



(Received 6 October 2022; revised 19 December 2022; accepted 5 January 2023; published 30 January 2023)

We report on a neutron diffraction study of single-crystal CePtAl₃ complemented by measurements of the specific heat under applied magnetic field. Below $T_N \approx 3$ K, CePtAl₃ develops incommensurate antiferromagnetic order with a single modulation vector $\mathbf{k} = (0.676\ 0\ 0)$. Residual magnetic scattering intensity above T_N and a broadening of the specific heat anomaly at T_N may be consistently described in terms of a Gaussian distribution of transition temperatures with a standard deviation $\sigma \approx 0.5$ K. The distribution of T_N may be attributed to the observation of occupational and positional disorder between the Pt and Al sites consistent with structural information inferred from neutron diffraction. Measurements under magnetic field reveal changes of the magnetic domain populations when the field is applied along the [0 1 0] direction consistent with a transition from cycloidal to amplitude-modulated magnetic order ~ 2.5 T.

DOI: [10.1103/PhysRevResearch.5.013058](https://doi.org/10.1103/PhysRevResearch.5.013058)

I. INTRODUCTION

Cerium-based intermetallics comprise a wide variety of physical phenomena owing to the coupling between electronic and magnetic degrees of freedom and their relationship to the crystal structure and its symmetry. Perhaps most extensively studied are materials with the ThCr₂Si₂ structure, featuring heavy fermion superconductivity, quantum phase transitions, as well as large magnetoelastic coupling phenomena [1,2]. Born out of this long history, a structurally related materials class that has attracted increasing interest in recent years comprises CeTX₃ systems, where T is a transition metal and $X =$ Al, Ga, Si, or Ge. For instance, in CeCuAl₃ and CeAuAl₃,

anomalous thermal transport properties and inelastic neutron and x-ray scattering experiments have revealed magnetoelastic hybrid excitations even for nominally weak magnetoelastic coupling [3–5]. Moreover, antiferromagnetic (AFM) order with low transition temperatures have been reported, e.g., for $T =$ Cu and Au, where CeCuAl₃ exhibits an amplitude modulated, collinear, AFM structure, with a modulation vector $\mathbf{k} = (\frac{2}{5}\ \frac{3}{5}\ 0)$ below $T_N = 2.7$ K [6], while CeAuAl₃ exhibits a helical AFM structure with $\mathbf{k} = (0\ 0\ 0.52)$ below $T_N = 1.2$ K [4].

A key aspect of the $I4mm$ space group, in which most members of the CeTX₃ class crystallize, is the presence of a fourfold symmetry axis along the [00 1] direction. For \mathbf{k} vectors in the basal plane as in CeCuAl₃, this permits, in principle, the formation of multi- k magnetic structures. This possibility was considered unlikely for CeCuAl₃ [6]; however, multi- k structures were observed in various other cerium intermetallics [7–9]. Thus, to unambiguously determine the magnetic state, the number of modulation vectors must be determined, and measurements under symmetry-breaking conditions must be performed to distinguish a

*michal.stekiel@frm2.tum.de; m.stekiel@fz-juelich.de

Published by the American Physical Society under the terms of the Creative Commons Attribution 4.0 International license. Further distribution of this work must maintain attribution to the author(s) and the published article's title, journal citation, and DOI.

potential multi- k structure from the formation of magnetic domains. On this note, the putative presence of multi- k order in the CeTAl₃ family would identify another exciting facet of correlated electron systems. Further, the low Néel temperatures in these systems suggest a possible vicinity to a quantum phase transition. This raises the question if other members of the CeTAl₃ family exist that are either nonmagnetic in the zero-temperature limit or even coincidentally located at a quantum critical point.

In this paper, we report the observation of long-range AFM order in CePtAl₃. This system crystallizes in the BaNiSn₃-type structure, with a noncentrosymmetric, tetragonal $I4mm$ space group [10]. Previous reports on the possible existence of long-range magnetic order in CePtAl₃ were inconclusive [10,11]. The electrical resistivity, magnetization, and specific heat of polycrystalline samples were found to be characteristic of spin-glass behavior <0.8 K [11]. However, the authors of that study noted [11] that their CePtAl₃ sample showed a high degree of crystalline disorder, speculating on an intrinsic lack of long-range magnetic order. Likewise, based on the electrical resistivity, Franz *et al.* [10] suggested that CePtAl₃ does not exhibit magnetic order down to 0.1 K. Moreover, the magnetization of single-crystal CePtAl₃ shows an almost linear magnetic field dependence up to 9 T [12], without signs of saturation. The magnetic moments at 9 T and 2 K are 1 and 0.3 μ_B for field applied along the a and c axes, respectively, which is far from the value expected for an isolated Ce³⁺ atom of 2.14 μ_B . This suggests the presence of crystal field effects that influence the magnetism in CePtAl₃ and establishes an easy magnetization plane (001) and a hard magnetic axis along the [001] direction. Taken together, these data suggested a possible vicinity to a quantum phase transition, motivating the detailed microscopic study reported in this paper.

II. EXPERIMENTAL METHODS

Centimeter-sized single crystals of CePtAl₃ were grown from polycrystalline rods using an optical floating-zone furnace, described in more detail in Refs. [12–14]. Both the stability of the floating-zone growth, which was well-behaved, and the metallurgical appearance of the ingot reject the possibility of macroscopic phase segregation. Rather, behavior characteristic of homogeneous sample was observed. The crystals reported in this paper were prepared from the same batch studied by Franz *et al.* [10]. Samples were cut from the single-crystalline rod as required for the different experimental techniques. Demagnetization effects were negligible for all samples studied. The specific heat was measured in a Quantum Design physical properties measurement system at temperatures down to 2 K under applied magnetic fields up to 14 T. Constant field scans as a function of temperature were performed on a $1 \times 1 \times 1$ mm³ single-crystal cube of CePtAl₃ using a large heat-pulse method. Constant temperature scans as a function of an applied magnetic field were carried out on a $2 \times 1 \times 6$ mm³ single crystal using a small heat-pulse method. In all specific heat measurements, the magnetic field was applied along the [100] direction. Neutron diffraction was carried out at several different beamlines using a large

cylinder-shaped crystal with a length and diameter of 12 and 6 mm, respectively (volume = 340 mm³).

Initial single-crystal neutron diffraction measurements were performed on the triple-axes-spectrometer PANDA [15] at the MLZ. The crystal was mounted in a ³He cryostat and cooled to 0.5 K. The intensities of selected reflections were measured as a function of temperature to investigate the magnetic transition. The modulation vector of the magnetic order was determined from measurements at the diffuse neutron scattering spectrometer (DNS) [16,17] at MLZ using polarization analysis. The incoming wavelength of 4.2 Å and the one-dimensional detector bank at the DNS allowed us to simultaneously collect data for a range of momentum transfers $0.25 < Q < 2.7$ Å⁻¹. The sample was rotated by 1° steps in a 140° range to map out the neutron scattering intensity on a plane in reciprocal space. Here, xyz -polarization analysis was employed with the neutron polarization set parallel to the momentum transfer, which allowed us to distinguish between magnetic and nuclear scattering contributions on the spin-flip (SF) and non-spin-flip (NSF) channels, respectively [18,19]. The crystal was cooled to 0.45 K using a ³He cryostat. Data were analyzed and reduced with the MANTID package [20] allowing us to project the measured intensities on selected crystal planes.

Further single-crystal neutron diffraction measurements were performed on POLI [21] at MLZ and on D23 [22] at the ILL. Both diffractometers operate a sample stage with an ω rotation axis and a lifting detector stage allowing us to measure out-of-plane scattering intensity. Measurements at POLI aimed at an accurate determination of the crystal structure.

To minimize extinction effects, a small half-disc-shaped crystal with dimensions 6×1 mm (diameter \times thickness) and a volume of 14 mm³ was used at an incoming wavelength of 3.355 Å. Data were first recorded at ambient conditions. Following this, the sample was mounted in the ³He cryostat and cooled to 0.45 K. Measurements at D23 aimed at the determination of the magnetic structure and were performed with a 6 T vertical field magnet at 1.5 K at an incoming wavelength of 1.275 Å. The same crystal that was used at the DNS and PANDA ($V = 340$ mm³) was mounted in two configurations, first with the [010] direction vertical and second with the [001] direction vertical.

The experimental protocol for measurements under magnetic field at D23 was as follows. The sample was cooled to 1.5 K in zero field, and the magnetic field was applied along the [010] direction, i.e., along the b axis. The field was ramped from $\mu_0 H = 0$ to 5.5 T and then down to $\mu_0 H = 0$ in steps. At each field, a series of Q and ω scans was measured to determine the position and intensity of selected reflections. Following this, the sample was heated to ambient temperature, reoriented, and cooled down to 1.5 K again, so that the magnetic field was applied along the [001] direction, i.e., along the c axis. For this orientation, we measured magnetic and nuclear reflections up to 4 T under increasing magnetic field. Integration of the reflections from the diffraction measurements was done with the DAVINCI program [23]. For the determination of magnetic structures, refinements were carried out using JANA2006 [24] with the symmetry analysis input from ISODISTORT [25].

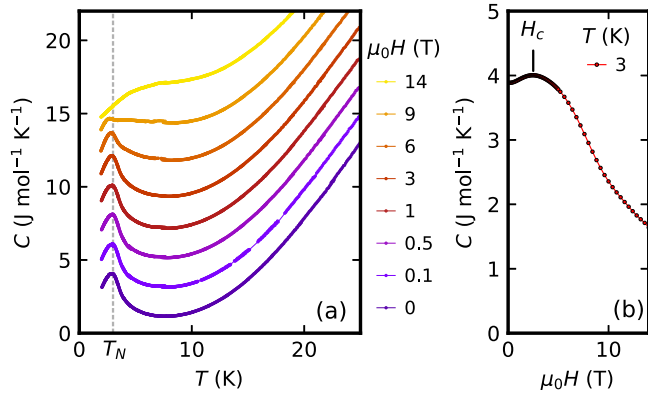


FIG. 1. Specific heat of CePtAl₃. (a) Specific heat as a function of temperature at various magnetic fields up to 14 T. Data are shifted vertically by 2 J/(mol K) for clarity. The dashed line marks characteristic temperature T_N at which the field sweep was measured as shown in (b). In (a), the maximum in specific heat at $T_N = 3$ K marks the transition to the magnetically ordered state, consistent with neutron scattering. (b) Specific heat as a function of magnetic field at $T = 3$ K. In (b), the local maximum of the 3 K field sweep is marked with H_c at 2.5 T and coincides with the magnetic transition observed with neutron scattering.

III. RESULTS AND INTERPRETATION

The presentation of our experimental results is organized as follows. The specific heat data are presented in Sec. III A. Following this, the results of four independent neutron diffraction measurements are reported. Measurements focusing on the accurate determination of the crystal structure are presented in Sec. III B. The results of the search for the magnetic modulation vector and the characterization of the magnetic order parameter are presented in Sec. III C. Finally, determination of the AFM order and its behavior under applied magnetic fields are reported in Sec. III D.

A. Specific heat

The specific heat of CePtAl₃ was measured as a function of temperature at various applied magnetic fields up to 14 T, as shown in Fig. 1, where we focused on the low-temperature part in the regime of the magnetic transition. At zero magnetic field, the specific heat shows a broad maximum centered at $T_N = 3$ K with a full width at half maximum (FWHM) of ~ 1.5 K. Under increasing applied field, there is no visible change in the specific heat curve up to 3 T. At 6 and 9 T, the amplitude of the maximum is decreased and slightly shifted toward lower temperatures. The maximum has vanished at 14 T.

The field dependence was explored further in measurements as a function of magnetic field at fixed temperature, as shown in Fig. 1(b). At 3 K, the specific heat exhibits a maximum at 2.5 T marked as H_c and a monotonic decrease under increasing field above H_c .

As shown below, neutron diffraction allows us to associate the broad maxima in the specific heat at 3 K and zero field with the transition to AFM order, while the local maximum at $\mu_0 H_c = 2.5$ T coincides with a field-driven magnetic transition.

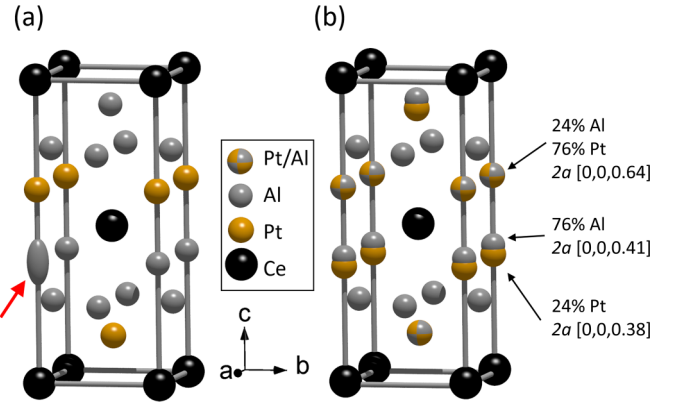


FIG. 2. Crystal structure of CePtAl₃. (a) Archetypal BaNiSn₃ structure. Red arrow in (a) points at the Al atom on the $2a$ site which exhibits strong elongation of displacement ellipsoid and is modeled by splitting the equivalent sites. (b) BaNiSn₃ structure modified with occupational and positional disorder on the Al $2a$ and Pt $2a$ sites. Occupations of the disordered sites and their positions are indicated by the labels.

B. Crystal structure

Single-crystal neutron diffraction at ambient conditions confirmed that CePtAl₃ crystallizes in the BaNiSn₃ structure with a noncentrosymmetric $I4mm$ space group, as previously reported by Franz *et al.* [10] and shown in Fig. 2. Lattice parameters and atomic positions are summarized in Table I. A large number of high- Q reflections allowed for a reliable refinement of the displacement parameters.

The refinement for the BaNiSn₃ structure showed negative displacement parameters on the Al $2a$ site and a rather high refinement quality factor $R_{\text{obs}} = 12.24$. The refinement was found to be improved, $R_{\text{obs}} = 5.67$, when assuming antisite disorder between the Al and Pt $2a$ sites. Further, the displace-

TABLE I. Details of the CePtAl₃ crystal structure refinement based on neutron diffraction at ambient temperature. Space group $I4mm$, $a = b = 4.326$ Å, $c = 10.655$ Å. The number of measured : independent : observed reflections is 343:175:156, where $R_{\text{int}} = 8.21$, and observed reflections are with $I > 3\sigma(I)$. The refinement was performed on F^2 with $R_{\text{obs}} = 4.98$ and $wR_{\text{obs}} = 11.11$. The columns contain the symbol of the Wyckoff site, atoms occupying the site, occupancy, z coordinate of the Wyckoff site ($2a$: [0, 0, z] and $4b$: [0, 0.5, z]), and associated, refined displacement parameters, respectively.

Site	Atom	Occupancy	z	U (Å ²)
$2a$	Ce	1	0 (fixed)	$U_{11} = 0.0168$ (17) $U_{33} = 0.0158$ (20)
	Pt	0.76	0.636 (1)	$U_{11} = 0.0126$ (12)
$2a$	Al	0.24		$U_{33} = 0.0157$ (12)
$2a$	Al	0.76	0.410 (1)	$U_{\text{iso}} = 0.0136$ (23)
	Pt	0.24	0.376 (2)	$U_{\text{iso}} = 0.0383$ (65)
$4b$	Al	1	0.251 (1)	$U_{11} = 0.0173$ (28)
				$U_{22} = 0.0172$ (28)
				$U_{33} = 0.0151$ (16)

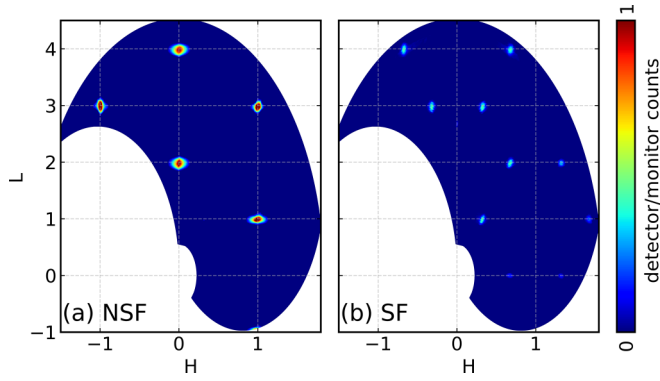


FIG. 3. Neutron diffraction intensity in the (HOL) plane of CePtAl_3 at 0.45 K. (a) Non-spin-flip (NSF) channel, where nuclear reflections are observed. (b) Spin-flip (SF) channel, where magnetic reflections with a modulation vector $\mathbf{k} = (0.676\ 0\ 0)$ are observed.

ment ellipsoid of the Al $2a$ site was found to be strongly elongated along the c axis, while other sites were found to show a fairly isotropic displacement, as illustrated in Fig. 2(a). This was taken as an indication of positional disorder. Splitting, in turn, the Al $2a$ site into separate sites occupied by Pt and Al atoms gave a final figure of merit $R_{\text{obs}} = 4.98$, where the occupancies were constrained to retain the stoichiometric composition of CePtAl_3 . Refinements without such a constraint did not improve the quality of the fit. The final model is summarized in Table I and illustrated in Fig. 2(b).

Cooling the crystal to 0.45 K, the intensities and positions of selected reflections were monitored to verify whether CePtAl_3 undergoes any structural modifications. No significant changes were seen, suggesting that the peak observed in the specific heat at 3 K is due to a magnetic transition that does not coincide with a strong response of the lattice. The intensities of the Bragg reflections also showed that the magnetic structure is characterized by a modulation vector $\mathbf{k} \neq 0$. The refinement of the 147 nuclear reflections measured at 0.45 K strongly favors the disorder model established at ambient temperature. The refined parameters are close to those listed in Table I, i.e., the crystal structure is identical at 0.45 K and ambient temperature, except for the displacement parameters, which at 0.45 K are reduced by a factor of two, as expected for low temperatures.

C. Spontaneous magnetic order

To determine the modulation vectors of the spontaneous magnetic order in CePtAl_3 , i.e., at zero magnetic field and low temperatures, we mapped the (HOL) plane in reciprocal space using neutron diffraction at 0.45 K. In addition to the nuclear reflections observed in the NSF channel, shown in Fig. 3(a), 10 weak magnetic reflections were detected in the SF channel, as shown in Fig. 3(b). The intensities of these magnetic reflections are roughly two orders of magnitude smaller than the nuclear reflections. They may be indexed by a modulation vector $\mathbf{k} = (0.676(4)\ 0\ 0)$. The value $k_x = 0.676(4)$ is close to commensurate order with $k_x = \frac{2}{3} = 0.\bar{6}$. However, further measurements confirmed that the modulation vector is, in fact, incommensurate.

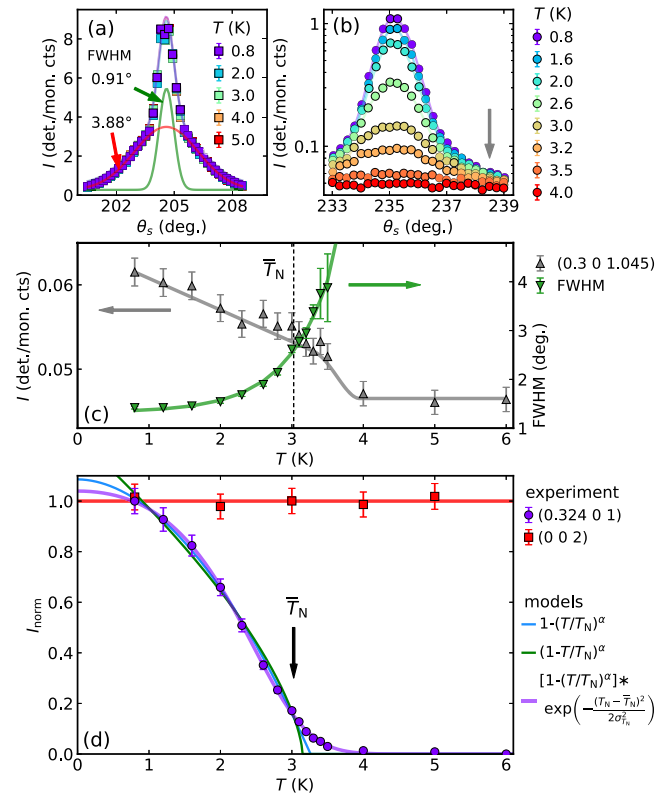


FIG. 4. Intensities of nuclear and magnetic reflections across the magnetic transition. (a) Nuclear $(0\ 0\ 2)$ reflection. It can be fitted with two Gaussian components (green and red lines) of different full widths at half maximum (FWHMs), as indicated by arrows and labels. (b) Magnetic $(0.324\ 0\ 1)$ reflection. In (a) and (b), data are shown with points, and solid lines are guides to the eye. (c) Intensity in the vicinity of the magnetic reflection (gray triangles) at the position marked with an arrow in (b) and the FWHM of the magnetic reflection (green triangles) as a function of temperature. (d) Integrated intensity of reflections in (a) and (b) as a function of temperature. The intensity of the magnetic reflection is not accurately reproduced with a power-law behavior (blue and green lines). A power-law dependence convoluted with a Gaussian distribution (solid, purple line) that may be attributed to the structural inhomogeneities in the sample provides the best fit.

The magnetic transition temperature was determined by means of neutron diffraction at PANDA. Upon cooling, the intensities of the magnetic and nuclear reflections at $(0.324\ 0\ 1)$ and $(0\ 0\ 2)$, respectively, were measured as shown in Fig. 4. Below 3.5 K, the intensity of the magnetic reflection increased, while the nuclear reflection did not change, indicating lack of an accompanying structural transition or sizable magnetostriction above the detection limit of our measurements, as mentioned in Sec. III B.

The nuclear reflection consisted of a sharp, resolution-limited diffraction peak with a FWHM of 0.91° . The additional presence of diffuse shoulders is well described by a broad Gaussian with $\text{FWHM} = 3.88^\circ$. We attribute the diffuse component to Huang scattering [26,27]. It arises from the atomic disorder, which causes strain fields responsible for broad, diffuse signal contributions around some Bragg reflections. In comparison, the shape of the magnetic reflection is

well described by a single Gaussian, without any qualitative change in line shape across the magnetic transition.

The temperature dependence of the intensity of the magnetic reflection may be equally well described by a power-law behavior $I \propto (1 - T/T_N)^\alpha$ and a modified, heuristic expression $I \propto 1 - (T/T_N)^\alpha$. Both functions are depicted in Fig. 4(c) together with the measured intensities. Neither fit includes a point of inflection that accounts for the residual intensity above T_N . Such residual intensity is commonly attributed to critical scattering that originates from slow, long-range correlations in the vicinity of the transition and gives rise to magnetic diffuse scattering. As a function of temperature, these correlations are most pronounced at the transition temperature [28,29]. In Fig. 4(c), the width of the magnetic reflection and the intensity in the vicinity of the magnetic reflection as a function of temperature are shown. The width of the reflection increased with increasing temperature, consistent with critical fluctuations. However, the magnetic diffuse intensity measured at the position marked with an arrow in Fig. 4(b), which corresponds to $(hkl) = (0.30\ 1.045)$, and shown in Fig. 4(c), did not exhibit a maximum around T_N . The diffuse scattering scales as the intensity of the magnetic reflection, suggesting static disorder of the long-range magnetic order rather than fluctuations with a specific Q dependence for the resolution of our setup. Considering the crystalline disorder characterized in Sec. III B, which reveals antisite disorder, the metallurgical appearance of our sample without hints for macroscopic phase segregation, and the broad peak in the specific heat, see Sec. III A, we suggest therefore an alternative explanation of the residual scattering intensity above T_N .

Namely, we propose that the atomic disorder and the structural inhomogeneities cause a spread of transition temperatures T_N that accounts for the residual scattering intensity above the transition, in addition to conventional critical scattering. The notion that structural inhomogeneities on the atomic scale may give rise to such a scattering contribution above the critical temperature was previously found to describe the magnetic transitions in polycrystalline samples of other materials [30,31]. Considering all information available, it represents perhaps the simplest scenario.

Incorporating the mathematical formalism reported by Reguński *et al.* [30], we describe the spread of the transition temperatures seen in neutron scattering by a Gaussian distribution, with an average transition temperature \bar{T}_N^n and a standard deviation $\sigma_{T_N}^n$. The measured intensity is then a convolution of the power-law behavior with the Gaussian distribution as depicted in Fig. 4(c). Using the modified power-law function $1 - (T/T_N)^\alpha$, which proved to be insensitive to the temperature range fitted, the model is in excellent agreement with experiment across the entire temperature range, where $\bar{T}_N^n = 3.03(15)$ K and $\sigma_{T_N}^n = 0.48(7)$ K. It is worthwhile to point out that the convoluted model assumes only one additional parameter than a power law, while significantly improving the quality of the fit.

The main conclusion suggested by this analysis also accounts for the broad signature in the specific heat shown in Fig. 1, using an analogous model where an underlying specific heat curve is convoluted by the distribution of transition temperatures determined in neutron scattering. Although the exact

parameterization of the specific heat is not straightforward, the width of the resulting convolution is dominated by the contribution from the distribution of transition temperatures [32], i.e., the resulting curve depends little on the precise form of the parameterization in the disorder-free compound. Notably, the transition temperature $\bar{T}_N^{c_p} = 3$ K and the FWHM of ~ 1.5 K, which corresponds to a standard deviation $\sigma_{T_N}^{c_p} = 0.64$ K observed in the specific heat, are very close to the values determined in neutron scattering, $\bar{T}_N^n = 3.03(15)$ K and $\sigma_{T_N}^n = 0.48(7)$ K.

D. Magnetic order under magnetic field

Various magnetic reflections were measured at 1.5 K as a function of magnetic field up to 5.5 T. The main observation inferred from these measurements is that the $(hkl) \pm (0.676\ 0\ 0)$ and $(hkl) \pm (0\ 0.676\ 0)$ families of magnetic reflections behave differently under applied magnetic field. The general trend may be illustrated by means of the $(0.324\ 0\ 1)$ and $(0\ 0.324\ 1)$ reflections shown in Fig. 5.

Under increasing magnetic field applied along the $[0\ 1\ 0]$ direction (blue symbols in Fig. 5), the intensity of the $(0\ 0.324\ 1)$ reflection increases and reaches a maximum with a plateau between 1 and 1.5 T. Further increasing the field reduces the intensity of the $(0\ 0.324\ 1)$ reflection, which vanishes >3 T up to 5.5 T, the highest field studied. Subsequently decreasing the field to 1 T (orange symbols in Fig. 5), the intensity displays some hysteresis, as highlighted by a curve guiding the eye. Below 1 T, the intensity of the $(0\ 0.324\ 1)$ reflection does not drop to the value observed prior to increasing the field. Instead, it remains high, with a small drop just before the magnetic field reaches zero.

The behavior observed so far is contrasted by the intensity of the $(0.324\ 0\ 1)$ reflection, which is shown in Fig. 5. Under increasing magnetic field applied along $[0\ 1\ 0]$, its intensity decreases almost to zero at 1 T, followed by an increase, reaching a maximum at 3 T, before slowly decreasing again when increasing the field further. Decreasing the field next reveals the reverse evolution of the intensity. Analogous to the $(0\ 0.324\ 1)$ reflection, the intensity does not increase to reach the value before changing the field but remains low with a small upturn just before the magnetic field reaches zero.

Turning now to the behavior for magnetic field along the $[0\ 0\ 1]$ direction (black symbols in Fig. 5), the evolution of both reflections $(0.324\ 0\ 1)$ and $(0\ 0.324\ 1)$ is the same. Both exhibit essentially the same intensity and a monotonic decrease up to 4 T.

It is important to note that we did not observe any changes of the magnetic modulation vector as such or widths of the magnetic reflections for all applied fields studied under both increasing and decreasing field. The magnetic modulation vector determined under applied fields is $\mathbf{k} = (0.677(1)\ 0\ 0)$, consistent with the value presented in Sec. III C. In addition, we did not observe significant intensity of the second-order mixed satellites, such as $(0.324\ 0.676\ 1)$ and others, that would be indicative of a multi- k magnetic structure. Instead, the field dependence of the magnetic reflections is clearly characteristic of the formation of a multidomain, single- k AFM structure.

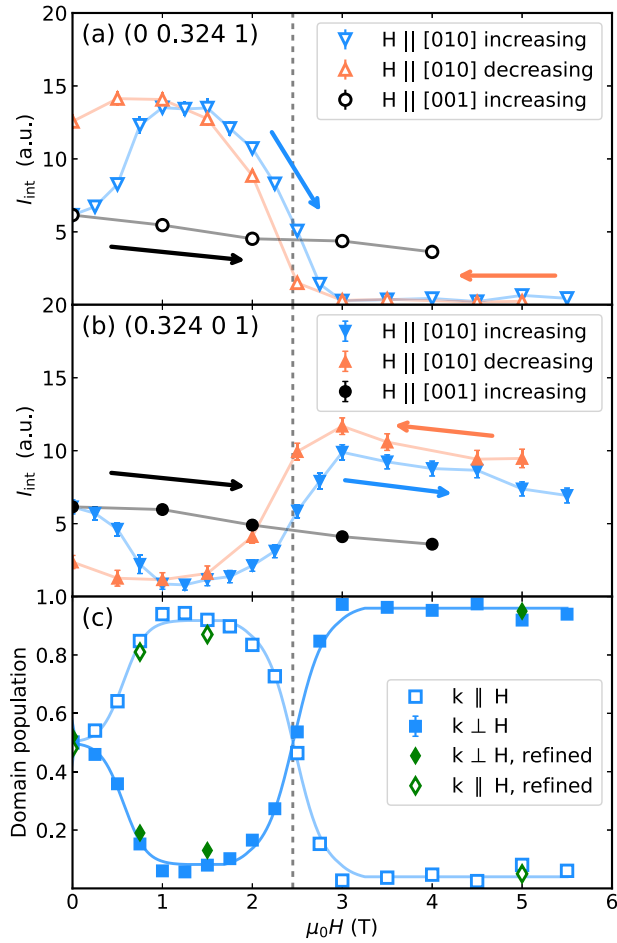


FIG. 5. Diffraction intensity as a function of magnetic field. Reflections were measured in increasing (blue) and decreasing (orange) field applied along the [010] axis and in increasing field applied along the [001] axis (open symbols). (a) Intensity of the (00.324 1) reflection (open symbols). (b) Intensity of the (0.324 0 1) reflection (closed symbols). (c) Domain populations as determined by scaling the intensities of reflections in (a) and (b) under increasing field applied along the [010] direction (blue squares) and determined from the refinement (green diamonds). Solid lines are guides to the eye. The vertical line marks the field of 2.5 T, the midpoint of domain repopulation.

Namely, for a single-domain, multi- k structure, the intensities of the (00.324 1) and (0.324 0 1) reflections would have to be the same in some field range, whereas a small field of order 0.25 T already changes the intensities of these reflections, as shown in Fig. 5. Further, up to 1 T, the magnetic field changes the domain population, almost saturating the volume of the domain with the magnetic modulation vector along the field direction ($\mathbf{k} \parallel \mathbf{H}$), related to the intensity of the (00.324 1) reflection.

Above 1.5 T, an unexpected exchange of intensity may be observed between the two reflections and a repopulation of the magnetic domains. Decreasing the field causes a hysteresis in the behavior of the intensities of the magnetic reflections. The difference of intensity after removing the applied magnetic field is, finally, characteristic of the presence of magnetic domains. Here, the relative intensities of the reflections allow us

TABLE II. Parameters obtained from fitting the intensity of the (0.324 0 1) magnetic reflection with different models shown in Fig. 4(c).

Model	Parameters	
$1 - (T/T_N)^\alpha$	$T_N = 3.26(3)$ K	$\alpha = 1.89(11)$
$(1 - T/T_N)^\alpha$	$T_N = 3.15(6)$ K	$\alpha = 0.66(5)$
$[1 - (T/T_N)^\alpha]^*$	$\bar{T}_N = 3.02(15)$ K	$\alpha = 2.7(8)$
$*\exp(-(T_N - \bar{T}_N)^2/2\sigma_{T_N}^2)$	$\sigma_{T_N} = 0.48(7)$ K	

to determine the field dependence of the domain populations, as shown in Fig. 5(c).

E. Real-space depiction of magnetic order

Establishing that CePtAl₃ exhibits a single- k magnetic structure allows us to infer the orientation of the magnetic moments in real space. The single- k character of the magnetic order lowers the symmetry of the tetragonal $I4mm$ space group to orthorhombic $Imm2$, where two irreducible representations σ_1 and σ_2 are allowed. For $\mathbf{k} = (0.676 0 0) = (k 0 0)$, labeled k_\perp since $\mathbf{k} \perp \mathbf{H} \parallel [0 1 0]$, the σ_1 representation describes an amplitude-modulated antiferromagnet with the magnetic moment associated with the Ce atom at Wyckoff position $[x, y, z]$:

$$\mathbf{m}_{\sigma_1}^{k_\perp}(\mathbf{r}) = [0, m_1 \sin(2\pi kx), 0]. \quad (1)$$

In comparison, the σ_2 representation describes a cycloidal modulation of magnetic moments in the ac plane, with a moment:

$$\mathbf{m}_{\sigma_2}^{k_\perp}(\mathbf{r}) = [m_2 \sin(2\pi kx), 0, m_3 \cos(2\pi kx)]. \quad (2)$$

The parameters m_i describe the amplitude modulation along different axes. They may be refined using the experimental data. Note that, for the other domain with $\mathbf{k} = (0 0.676 0)$ labeled k_\parallel , the modulation vector direction is different, and the magnetic moments are given by

$$\mathbf{m}_{\sigma_1}^{k_\parallel}(\mathbf{r}) = [m_1 \sin(2\pi ky), 0, 0], \quad (3)$$

and

$$\mathbf{m}_{\sigma_2}^{k_\parallel}(\mathbf{r}) = [0, m_2 \sin(2\pi ky), m_3 \cos(2\pi ky)]. \quad (4)$$

The refinement of the dataset collected at $\mu_0 H = 0, 0.75$, and 1.5 T strongly supports a cycloidal structure, where the refined magnetic moment components are listed in Table III, and the arrangement of the moments in real space is shown in Fig. 6. For the data collected at 5 T, the refinement is not conclusive, and both cycloidal and amplitude-modulated magnetic structures account for the data equally well.

One of the causes of this uncertainty may be the relatively small number of reflections measured. For the cycloidal model, the m_3 parameter, which is the modulation amplitude along the c axis, is poorly constrained, and the best refinement is obtained when setting it to zero. As a result, at 5 T, both models correspond to the amplitude-modulated magnetic structure with moments lying either along the b or a crystal axis, for the σ_1 and σ_2 models, respectively, as shown in Fig. 6.

TABLE III. Parameters of the CePtAl₃ magnetic structure determined from diffraction measurements at high magnetic field applied along the [0 1 0] direction. Consecutive columns correspond to the magnetic field, domain population ratio, goodness of fit (GOF), R factor for magnetic satellites, chosen representation, and magnetic moment components.

$\mu_0 H$ (T)	$k_{\perp} : k_{\parallel}$	GOF	R_{sat}	Repr.	m_i (μ_B)
0	52:48	4.89	12.15	σ_2	$m_2 = 0.852$ (25) $m_3 = 0.484$ (37)
0.75	19:81	9.25	14.75	σ_2	$m_2 = 0.836$ (82) $m_3 = 0.494$ (130)
1.5	13:87	8.44	16.71	σ_2	$m_2 = 0.846$ (77) $m_3 = 0.52$ (12)
5	95:5	13.5	8.99	σ_1	$m_1 = 0.64$ (15)
5	95:5	13.62	8.12	σ_2	$m_2 = 0.65$ (16) $m_3 = 0$ (0.5)

Since high magnetic fields tend to align the microscopic magnetic moments along the field direction, the model with the σ_1 representation seems more likely. However, further investigations will be necessary to resolve these uncertainties.

F. Further discussion

The evolution of the magnetic structure in CePtAl₃ under magnetic field applied along the [0 1 0] direction may be summarized as follows. At $\mu_0 H = 0$, two equally populated magnetic domains coexist, supporting cycloidal magnetic order described by Eqs. (2) and (4). One domain exhibits a modulation vector $\mathbf{k}_{\perp} = (0.676\ 0\ 0)$, while the other exhibits $\mathbf{k}_{\parallel} = (0\ 0.676\ 0)$.

Application of the magnetic field along the [0 1 0] direction changes the domain populations, initially favoring the domain with $\mathbf{k}_{\parallel} = (0\ 0.676\ 0)$. This domain population becomes saturated between 1 and 1.5 T, where the magnetic moments are described by Eq. (4), as depicted in Figs. 6(a) and 6(b). Further, between 1.5 and 3 T, an exchange of the intensity is observed between the magnetic reflections with \mathbf{k}_{\parallel} and \mathbf{k}_{\perp} , as shown in Fig. 5(c), corresponding to a domain repopulation. This repopulation of the domains is associated with a transition to an amplitude-modulated structure, where the moments are either oriented along [1 0 0] or [0 1 0] with a modulation amplitude $m \approx 0.65 \mu_B$. In contrast, when the magnetic field was applied along [0 0 1], we did not see any evidence suggesting a reorientation of the magnetic moments, and the domains remained equally populated at all applied magnetic fields.

For magnetic field exceeding 3 T, the intensities of the magnetic reflections decreased monotonically with increasing field for both field directions. This is consistent with a reduction of the modulation amplitude and the increase of the uniform magnetization detected in the magnetization [12]. Indeed, we observed an increase of intensity at specific $\mathbf{k} = 0$ reflections, reflecting the uniform magnetization in the scattering process. Moreover, for field applied along the [0 1 0] direction, the magnetization measured at 2 K and

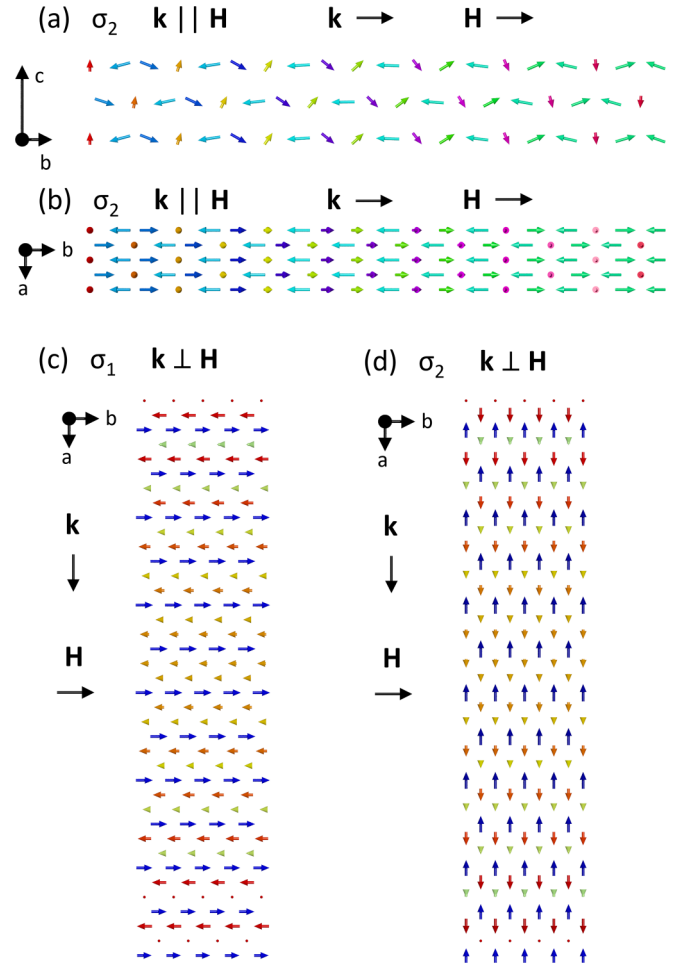


FIG. 6. Depiction of the incommensurate component of the magnetic order of CePtAl₃ under applied magnetic field. (a) and (b) Cycloidal phase with $\mathbf{k} \parallel \mathbf{H}$ observed < 2.5 T, viewed along (a) the [1 0 0] direction and (b) the [0 0 1] direction. (c) and (d) Amplitude-modulated phase with $\mathbf{k} \perp \mathbf{H}$ observed between 2.5 and 5.5 T with the moments oriented along (c) the [0 1 0] direction or (d) the [1 0 0] direction; view along the [0 0 1] direction (c axis). On the left-hand side of each panel, a coordinate system is shown which corresponds to the size of a nuclear unit cell. Next to each panel, the directions of the modulation vector \mathbf{k} and the applied magnetic field \mathbf{H} are shown. For the cycloidal structure, colors mark the azimuthal angle between the magnetic moment and the [0 0 1] direction. For the amplitude-modulated structure, colors mark the modulus of the magnetic moment.

5 T of $0.75 \mu_B$ per cerium atom [12] was of the same order of magnitude as the amplitude of the modulation, $m_3 = 0.65 \mu_B$, inferred from our neutron diffraction measurements. Overall, the magnetic structure is consistent with the magnetic anisotropies determined from previous measurements [10,12], which establish an easy magnetization plane (0 0 1) and a hard magnetic axis along the [0 0 1] direction, since the main components of the modulated part of the magnetization lie in the (0 0 1) plane, as summarized in Table III.

Most likely, the tilting of the magnetic moment away from the easy (0 0 1) plane is the result of Dzyaloshinskii-Moriya interactions allowed for the noncentrosymmetric $I4mm$ space group, see table II in Ref. [33]. Alternatively, the field

dependence may suggest coexisting local and itinerant magnetism in CePtAl₃, as reported for other cerium compounds [34,35], where the itinerant electrons might carry the magnetic moment component along the *c* axis, driving the incommensurability of the magnetic order.

Within the experimental resolution of our study, we did not observe any changes in the length scales of the magnetic modulations reflected in the constant component of the modulation vector $k = 0.677(1)$ under applied field. Our experimental setup allowed us to clearly distinguish that the modulation is not commensurate with $k = \frac{2}{3}$. The mechanism causing the formation of the incommensurability and the pinning of the magnetic modulation length cannot be explored further in our study. Since it is unchanged for both field directions and up to relatively high magnetic fields, it seems possible that the pinning involves structural disorder and follows the underlying atomic length scales of the disorder.

IV. CONCLUSIONS

In conclusion, we reported on a detailed neutron diffraction study of the crystal and magnetic structure of CePtAl₃ complemented by specific heat measurements. For our study, we have grown a large single crystal of CePtAl₃ by means of optical floating zone, which exhibits occupational and positional disorder on atomic length scales in neutron diffraction measurements. In the simplest scenario, the disorder affects the long-range magnetic order, which is described well in terms of a spread of the transition temperatures with an average transition temperature $\overline{T}_N^m = 3.03(15)$ K and standard deviation $\sigma_{T_N^m}^m = 0.48(7)$ K. This model is quantitatively consistent between the temperature dependence of the magnetic order parameter observed in neutron diffraction and the distribution of anomalies in the specific heat at the magnetic transition where $\overline{T}_N^{c_p} = 3$ K and $\sigma_{T_N^{c_p}}^{c_p} = 0.64$ K.

Measurements under applied magnetic field provided further information on the magnetic structure of CePtAl₃. For fields up to 1 T applied along [0 1 0], CePtAl₃ exhibits the characteristics of a multidomain state with single-*k*, incommensurate, cycloidal magnetic order. Between 1 and 1.5 T, a single domain state is stable. Further increasing the field

causes a magnetic transition between 1.5 and 3 T, suggesting a change from cycloidal to amplitude-modulated magnetic order. Above 3 T, the magnetic order may be described by amplitude-modulated moments in the tetragonal plane. For fields applied along [0 0 1], no transitions were observed, and CePtAl₃ remains in a multidomain state up to 4 T, the highest field studied. Putative mechanisms at the heart of the AFM order may be Dzyaloshinskii-Moriya spin-orbit interactions or, more speculatively, a mixed itinerant and local-moment magnetism carried by the conduction and *4f* electrons, respectively.

Taken together, the evidence for structural disorder and smearing of the magnetic phase transition in CePtAl₃ at zero magnetic field and the magnetic field dependence of the AFM structure from cycloidal to amplitude-modulated order identify a highly unusual interplay of magnetic order, magnetic textures, and structural properties in the presence of disorder in an *f*-electron compound.

ACKNOWLEDGMENTS

We kindly acknowledge Thomas Müller for help with the analysis of the DNS data, Alistair Cameron for support at D23, as well as Marc Wilde and Vivek Kumar for helpful discussions. We also thank the staff at the MLZ and ILL for support. Parts of the neutron measurements were performed at POLI, jointly operated by the RWTH Aachen University and JCNS within the JARA-FIT collaboration.

This study was funded by the Deutsche Forschungsgemeinschaft under Project No. WI33203-1, TRR80 (From Electronic Correlations to Functionality, Project No. 107745057, Project E1), SPP2137 (Skyrmionics, Project No. 403191981, Grant No. PF393/19), and the excellence cluster MCQST under Germany's Excellence Strategy EXC-2111 (Project No. 390814868). Financial support by the European Research Council through Advanced Grants No. 291079 (TOPFIT) and No. 788031 (ExQuiSid) and through the European Union's Horizon 2020 research and innovation program as well as the Czech Science Foundation GAČR under the Junior Star Grant No. 21-24965M (MaMBA) is gratefully acknowledged.

-
- [1] M. Shatruk, ThCr₂Si₂ structure type: The perovskite of intermetallics, *J. Solid State Chem.* **272**, 198 (2019).
 - [2] C. Pfleiderer, Superconducting phases of *f*-electron compounds, *Rev. Mod. Phys.* **81**, 1551 (2009).
 - [3] S. Paschen, E. Felder, and H. R. Ott, Transport and thermodynamic properties of CeAuAl₃, *Eur. Phys. J. B* **2**, 169 (1998).
 - [4] D. T. Adroja, C. De La Fuente, A. Fraile, A. D. Hillier, A. Daoud-Aladine, W. Kockelmann, J. W. Taylor, M. M. Koza, E. Burzuri, F. Luis, *et al.*, Muon spin rotation and neutron scattering study of the noncentrosymmetric tetragonal compound CeAuAl₃, *Phys. Rev. B* **91**, 134425 (2015).
 - [5] P. Čermák, A. Schneidewind, Be. Liu, M.-M. Koza, C. Franz, R. Schönmann, O. Sobolev, and C. Pfleiderer, Magnetoelastic hybrid excitations in CeAuAl₃, *Proc. Natl. Acad. Sci. USA* **116**, 6695 (2019).
 - [6] M. Klicpera, P. Javorský, P. Čermák, A. Schneidewind, B. Ouladdiaf, and M. Diviš, Neutron scattering study of magnetic order in single-crystalline CeCuAl₃, *Phys. Rev. B* **91**, 224419 (2015).
 - [7] J. Schweizer, F. Givord, J. X. Boucherle, F. Bourdarot, and E. Ressouche, The accurate magnetic structure of CeAl₂ at various temperatures in the ordered state, *J. Phys.: Condens. Matter* **20**, 135204 (2008).
 - [8] P. Puphal, V. Pomjakushin, N. Kanazawa, V. Ukleev, D. J. Gawryluk, J. Ma, M. Naamneh, N.-C. Plumb, L. Keller, R. Cubitt, *et al.*, Topological Magnetic Phase in the Candidate Weyl Semimetal CeAlGe, *Phys. Rev. Lett.* **124**, 017202 (2020).
 - [9] A. Donni, A. Furrer, P. Fischer, S. M. Hayden, F. Hulliger, and T. Suzuki, Magnetic properties of the dense Kondo compound CeSe studied by neutron scattering, *J. Phys.: Condens. Matter* **5**, 1119 (1993).

- [10] C. Franz, A. Senyshyn, A. Regnat, C. Duvinage, R. Schönmann, A. Bauer, Y. Prots, L. Akselrud, V. Hlukhyy, V. Baran, *et al.*, Single crystal growth of CeTAl₃ ($T = \text{Cu, Ag, Au, Pd and Pt}$), *J. Alloys Compd.* **688**, 978 (2016).
- [11] S. Mock, C. Pfleiderer, and H. V. Löhneysen, Low-temperature properties of CeTAl₃ ($T = \text{Au, Cu, Pt}$) and CeAuGa₃, *J. Low Temp. Phys.* **115**, 1 (1999).
- [12] C. Franz, *Untersuchung von Quantenphasenübergängen bei fehlender Inversionssymmetrie*, Dissertation, Technische Universität München, München, 2014.
- [13] A. Neubauer, J. Bœuf, A. Bauer, B. Russ, H. v. Löhneysen, and C. Pfleiderer, Ultra-high vacuum compatible image furnace, *Rev. Sci. Instrum.* **82**, 013902 (2011).
- [14] A. Bauer, G. Benka, A. Regnat, C. Franz, and C. Pfleiderer, Ultra-high vacuum compatible preparation chain for intermetallic compounds, *Rev. Sci. Instrum.* **87**, 113902 (2016).
- [15] A. Schneidewind and P. Čermák, PANDA: Cold three axes spectrometer, *JLSRF* **1**, A12 (2015).
- [16] Y. Su, K. Nemkovskiy, and S. Demirdiř, DNS: Diffuse scattering neutron time-of-flight spectrometer, *JLSRF* **1**, A27 (2015).
- [17] W. Schweika and P. Böni, The instrument DNS: polarization analysis for diffuse neutron scattering, *Phys. B: Condens. Matter* **297**, 155 (2001).
- [18] W. Schweika, XYZ-polarisation analysis of diffuse magnetic neutron scattering from single crystal, *J. Phys.: Conf. Ser.* **211**, 012026 (2010).
- [19] A. Boothroyd, *Principles of Neutron Scattering from Condensed Matter* (Oxford University Press, Oxford, 2020).
- [20] O. Arnold, J. C. Bilheux, J. M. Borreguero, A. Buts, S. I. Campbell, L. Chapon, M. Doucet, N. Draper, R. Ferraz Leal, M. A. Gigg, *et al.*, MANTID—Data analysis and visualization package for neutron scattering and μSR experiments, *Nucl. Instrum. Methods Phys. Res., Sect. A* **764**, 156 (2014).
- [21] V. Hutanu, POLI: Polarised hot neutron diffractometer, *JLSRF* **1**, A16 (2015).
- [22] E. Ressouche, J. Chiapusio, B. Longuet, F. Mantegazza, and J. Flouquet, The new thermal-neutron diffractometer D23, Institute Laue-Langevin (ILL), ILL Technical Report FR9903384, 1999.
- [23] A. Sazonov, DAVINCI: A scientific software for the visualization and processing of single-crystal diffraction data measured with a point detector, 2018. <http://davinci.sazonov.org/index.html>.
- [24] V. Petříček, M. Dušek, and L. Palatinus, Crystallographic Computing System JANA2006: General features, *Z. Kristallogr.* **229**, 345 (2014).
- [25] H. T. Stokes, D. M. Hatch, and B. J. Campbell, ISODISTORT, ISOTROPY Software Suite, 2022. <https://iso.byu.edu>.
- [26] K. Huang, X-ray reflections from dilute solid solutions, In *Selected Papers Of Kun Huang: (With Commentary)* (World Scientific, Singapore, 2000), pp. 1–16.
- [27] H. Peisl, Diffuse x-ray scattering from the displacement field of point defects and defect clusters, *J. Appl. Crystallogr.* **8**, 143 (1975).
- [28] M. K. Wilkinson and C. G. Shull, Neutron diffraction studies on iron at high temperatures, *Phys. Rev.* **103**, 516 (1956).
- [29] M. A. Krivoglaz, *Diffuse Scattering of X-Rays and Neutrons by Fluctuations* (Springer-Verlag, Berlin, Heidelberg, 1996).
- [30] M. Regulski, R. Przenioso, I. Sosnowska, and J.-U. Hoffmann, Short and long range magnetic ordering in $\beta\text{-MnO}_2$ —A Temperature Study, *J. Phys. Soc. Jpn.* **73**, 3444 (2004).
- [31] A.-F. Manchón-Gordón, R. López-Martín, A. Vidal-Crespo, J.-J. Ipus, J.-S. Blázquez, C.-F. Conde, and A. Conde, Distribution of transition temperatures in magnetic transformations: Sources, effects and procedures to extract information from experimental data, *Metals* **10**, 226 (2020).
- [32] Convolution of two Gaussians with variance σ^2 and τ^2 , results in a Gaussian with variance $\sigma^2 + \tau^2$. A broad contribution from a distribution of transition temperatures will hence dominate the convoluted Gaussian.
- [33] A. Bauer, A. Senyshyn, R. Bozhanova, W. Simeth, C. Franz, S. Gottlieb-Schönmeyer, M. Meven, T. E. Schrader, and C. Pfleiderer, Magnetic properties of the noncentrosymmetric tetragonal antiferromagnet EuPtSi₃, *Phys. Rev. Mater.* **6**, 034406 (2022).
- [34] T. Nakano, S. Onuma, N. Takeda, K. Uhlřřová, J. Prokleřka, V. Sechovský, J. Gouchi, and Y. Uwatoko, Coexistence of localized and heavy itinerant states in antiferromagnetic CePtGe₂, *Phys. Rev. B* **100**, 035107 (2019).
- [35] S. Hoshino and Y. Kuramoto, Itinerant Versus Localized Heavy-Electron Magnetism, *Phys. Rev. Lett.* **111**, 026401 (2013).